Low-Cycle Fatigue Properties of Ti6Al4V Laser-Welded Joints Based on a Local Strain Approach

Zhenzhen Xu, Jianxun Zhang, Wenke Wang, and Pinpin Sun

The low-cycle fatigue (LCF) properties of Ti6Al4V and laser-welded joints with different welding speeds are studied using smooth and notched flat specimens. A local strain approach is proposed to estimate the LCF properties of the notched flat specimen based on elastic–plastic finite element analysis (EPFEA). The local strain used in the approach is defined as the average strain in the plastic zone at the notch root and critical section of the notched flat specimen. The results indicate that the local strain approach is suitable for estimating the LCF properties of the notched flat Ti6Al4V titanium alloy specimen. The stress–strain relationship derived from the microhardness can be used in the EPFEA. The LCF properties of the Ti6Al4V laser-welded joints are worse in the heat-affected zone (HAZ) than in the base metal (BM) due to the martensite structure in the HAZ and the mechanical heterogeneity in the welded joints. The LCF properties of the Ti6Al4V laser-welded joints with different welding speeds are close under low strain levels and worse with higher welding speeds under high strain levels.

1. Introduction

Welded structures made of titanium and its alloys have been widely used in pressure vessels, rail vehicles, aerospace applications, large equipment and other manufacturing industries under dynamic loads. The laser welding of titanium alloys has drawn extensive attention from many studies due to the advantages of narrow weld beads, small distortions, high efficiency and good repeatability. Ti6Al4V titanium alloy has a dual-phase microstructure consisting of an equiaxed α phase and an intergranular β phase. The weld metal (WM) microstructure of Ti6Al4V laser-welded joints is mainly acicular martensite α'. The martensite α' and α phases are formed as hexagonal close-packed structures, which makes plastic deformation more difficult than in body-centered and face-centered cubic structures. The β phase is formed as a body-centered cubic structure. Moreover, the lattice distortion of the martensite α' phase is larger than that of the α phase. Therefore, the microhardness and strength of the WM are higher than those of the base metal (BM) in Ti6Al4V laser-welded joints, whereas the elongation at fracture is lower (Ref 1). Contamination in the WM of Ti6Al4V laser-welded joints can also cause an increase in the strength and a decrease in the ductility of the WM compared with the BM (Ref 2). Welding defects, such as underfills and undercuts, greatly affect the mechanical properties of laser-welded joints in titanium alloys. Underfill defects in a titanium laser-welded joint can cause a

loss of tensile strength. The fatigue properties of laser-welded joints in titanium alloys are inferior to those of undercut defects and worsen with increasing undercut size (Ref 3, 4). Welding parameters such as the welding speed have a great influence on the weld shapes and mechanical properties of laser-welded joints in titanium alloys. Köse et al. (Ref 5) noted a higher strength and lower ductility in Ti6Al4V laser-welded joints when using a high welding speed. Liu et al. (Ref 6) noted fractured fatigue specimens in the weld metal in Ti6Al4V laser-welded joints, an increased fatigue life with increasing heat input under load control, and a stress ratio of 0.1 after undercut defects were eliminated.

Normally, a low-cycle fatigue (LCF) assessment for titanium welded joints usually adopts smooth flat specimens with uniform gauge sections and nominal strain, which is appropriate for quickly finding the weak zone of a welded joint (Ref 7). However, a smooth flat specimen is not useful for measuring the LCF properties, such as the heat-affected zone (HAZ), of a designated area in a welded joint, but a notched flat specimen can be utilized. A nominal approach, as one of the global fatigue assessment approaches, neglects the structural details but divides the structures into different fatigue classes, which is the most widely used approach in situations of practical interest (Ref 8, 9). However, a nominal approach has limitations in the fatigue assessment of intricate components, and it is difficult to determine the nominal cross-section in complex welded joints that cannot be assigned to a specific fatigue class. These local approaches consider the local stress and strain concentrations for notched and welded components. The critical distance approach, as a local approach, is often used in the prediction of high cycle fatigue strength in notched Ti6Al4V components (Ref 10, 11). In a low-cycle fatigue region, the Manson–Coffin law considers the relationships among elastic strain, plastic strain and fatigue life, and it is widely used in the prediction of LCF life for notched specimens (Ref 12). The strains near the notch root can be obtained using a strain gauge (Ref 13), the digital image correlation (DIC) method (Ref 14, 15) and elastic–plastic finite element analysis (EPFEA). Karabulut et al. (Ref 16) verified that the fatigue results of cruciform-welded

Zhenzhen Xu, Jianxun Zhang, Wenke Wang, and **Pinpin Sun**, State Key Laboratory for Mechanical Behavior of Materials, Xi'an Jiaotong University, Xi'an 710049, China. Contact e-mail: jxzhang@mail.xjtu.edu.cn.

duplex stainless steel were consistent using hot spot stresses measured by strain gauges, the DIC method and EPFEA calculations. The stress–strain relationship used in EPFEA could be obtained from the microhardness of materials exhibiting power-law strain hardening (Ref 17-19).

In this paper, the LCF properties of Ti6Al4V laser-welded joints with different welding speeds were studied using smooth and notched flat specimens. EPFEA was adopted to calculate the strain distribution in the notched flat specimen while considering the differences in the constitutive relation in the welded joint. Based on EPFEA, a local strain approach was proposed to estimate the LCF properties for the notched flat specimen. Then, the LCF properties of Ti6Al4V and its laser-welded joints were analyzed thoroughly.

2. Materials and Experimental Procedures

The material studied herein was Ti6Al4V titanium alloy with a chemical composition (in wt.%) of Al = 5.90, V = 4.00, Fe = 0.20, O = 0.15, C = 0.05, N = 0.03, H = 0.01, and balance Ti. Mill-annealed Ti6Al4V plates with a thickness of 4 mm were prepared through sanding and acid cleaning before welding. Then, the plates were butt-welded by an IPG YLS-4000 fiber laser welding machine combined with a YASKAWA MOTOMAN welding robot, as shown in Fig. 1(a). A schematic diagram of the fixture and shielding delivery device is shown in Fig. 1(b). The shielding gas was argon with a purity of 99.99%. The flow rates of the shielding gas were 25, 25 and 15 L/min at the top, front and bottom of the welding plate, respectively. Laser welding for the Ti6Al4V was carried out with a laser power of 4000 W, a focal position of 6 mm, and welding speeds of 1.0, 1.5 and 2.0 m/min. After welding, the weld reinforcements and undercut defects were removed.

Two kinds of flat specimens were used in the LCF tests: a smooth flat specimen with a uniform gauge section, referred to as the smooth flat specimen, and a notched flat specimen, as shown in Fig. 2. All the fatigue specimens were mechanically polished to the same surface roughness. The LCF tests for the Ti6Al4V and its laser-welded joints were carried out at room temperature in tension-compression mode with a triangular load waveform with a strain rate of 0.004 s^{-1}, a strain ratio of -1, and a strain amplitude range of 0.5-1.6%. The measuring range of the strain gauge was 12.5 mm. The LCF tests were controlled by the nominal strain measured by the strain gauge.

3. Results and Discussion

3.1 The Microstructures and Mechanical Properties

It can be seen from the cross sections shown in Fig. 3 that the WM and HAZ widths change with the welding speed. The microstructures in the Ti6Al4V laser-welded joint are shown in Fig. 4. The microstructures of the BM are an equiaxed original α phase and an intergranular original β phase. The black dot in Fig. 4(a) and (b) is the original β phase, while the white equiaxed phase in Fig. 4(a) and (b) is the original α phase. The microstructure of the WM and fully transformed heat-affected zone (FTHAZ) is mainly an acicular martensite α′ phase. The grains in the WM are columnar grains, while the grains in the FTHAZ are equiaxed grains, as shown in Fig. 4(c) and (e). The microstructures of the partially transformed heat-affected zone (PTHAZ) are acicular martensite α′, blocky transformed α, equiaxed original α, and intergranular original β phases. The irregular blocky phase in Fig. 4(g) and (h) is the transformed α phase. The length of the martensite in the WM is the longest, and the length of the martensite in the PTHAZ is the shortest (Ref 20).

The Vickers microhardness was measured on a line 0.3 mm from the top surface of the cross sections of the welded joints shown in Fig. 3 under a test load of 500 g and dwell time of 15 s. Fig. 5 shows the distribution of the Vickers microhardness of the welded joints. The Vickers microhardness of the WM and FTHAZ is higher than that of the BM, and the microhardness of the FTHAZ is slightly higher than that of the WM, mainly because of the effects of the martensite structure in the WM and FTHAZ. The microhardness of the WM increases with increasing welding speed, which is consistent with the tendency of the strength described by Köse et al. (Ref 5).

The stress–strain relationship of the welded joint is difficult to obtain from the experiments, in particular the HAZ, because of the narrow width. The stress–strain relationship can be
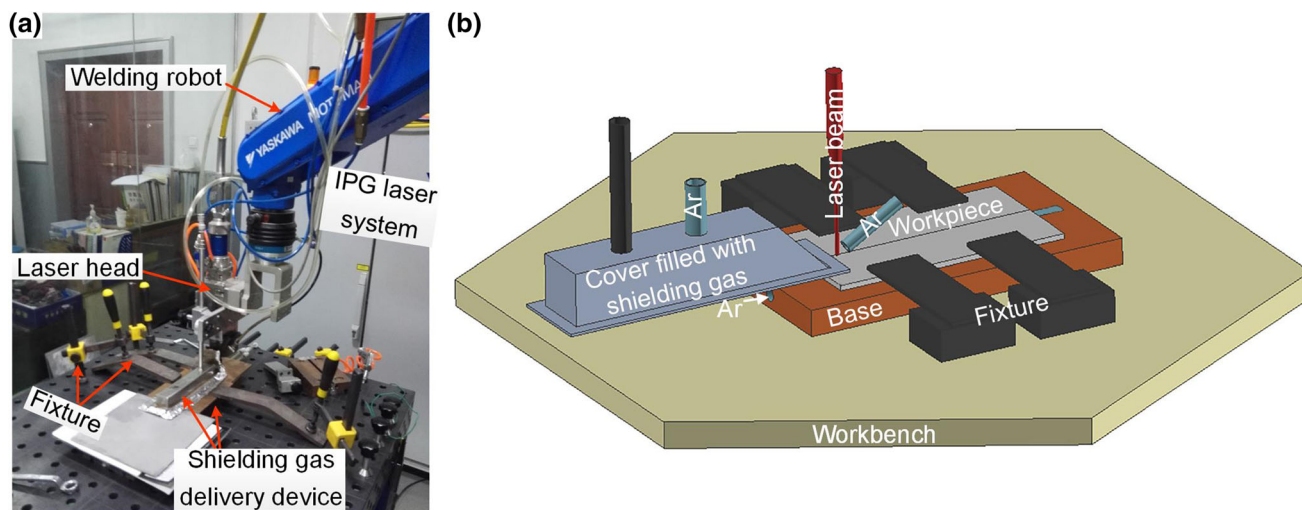

Fig. 1 Laser welding setup for Ti6Al4V: (a) experimental equipment; (b) schematic diagram of the fixture and shielding device
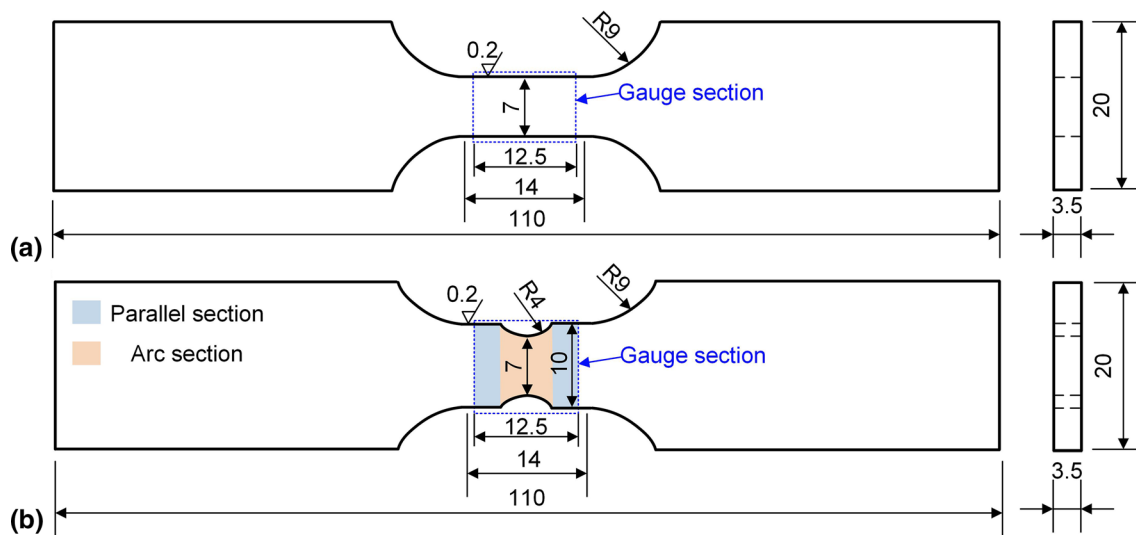
Fig. 2 Two kinds of flat specimens used in LCF tests: (a) the smooth flat specimen and (b) the notched flat specimen
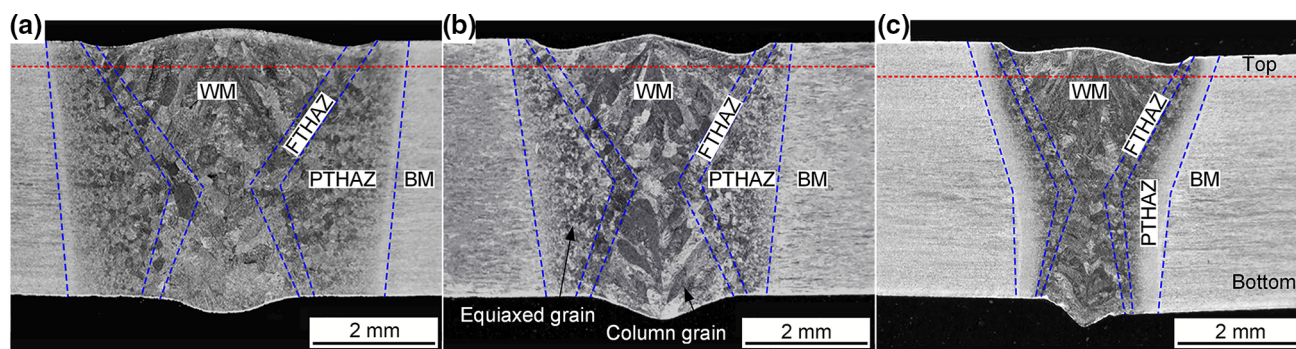

Fig. 3 Cross sections of the welded joints. The welding speed is (a) 1.0 m/min, (b) 1.5 m/min, and (c) 2.0 m/min

obtained from the microhardness, including the yield strength and strain hardening exponent. Keist et al. (Ref 18) demonstrated that a linear relationship $\left(\sigma_y = \frac{H_V}{3.60} - 90\right)$ between the yield strength σ_y and microhardness H_V could be developed for Ti6Al4V. For materials that exhibit power-law strain hardening, the relationship between the strain hardening exponent n, yield strength σ_y, and microhardness H_V was proposed by Cahoon et al. (Ref 21). The elastic modulus of the welded joints is regarded as the same as the elastic modulus of the BM (112 GPa) because the laser welding of Ti6Al4V is autogenous herein:

$$n = \frac{\log_{10}\left(\frac{3\sigma_y}{H_V}\right)}{\log_{10}\left(\frac{12.5\sigma_y}{E}\right)} \qquad \text{(Eq 1)}$$

where H_V is the Vickers microhardness (MPa) and E is the elastic modulus (MPa).

3.2 The Definition of the Local Strain Approach

Because crack initiation and propagation depend largely on the local strain near the notch root, the LCF properties of the notched flat specimen are assessed by the local strains near the notch root. A local strain approach is proposed to estimate the LCF properties for the notched flat specimen, and the local strain is defined as the average strain in the plastic zone and

critical section of the notched specimen, as indicated by line EP in Fig. 6. The section EFGH in Fig. 6 is regarded as the critical section in which cracks propagate. The length of line EP equals the depth of the plastic zone. The local strain changes with the variation in the fatigue load. The strain distribution of the notched flat specimen can be calculated by the EPFEM. The notched flat specimen is symmetric about the middle plane, so only one side of the plastic zone is taken for calculation. Point E is located at the maximum strain point along the notch root and is regarded as the location of crack initiation.

3.3 The LCF Properties of Ti6Al4V Titanium Alloy

The local strain approach is applied to estimate the LCF properties of the notched flat specimen of Ti6Al4V titanium alloy. The gauge section of the notched flat specimen shown in Fig. 2(b) includes a parallel section and an arc section. The arc section causes the fracture to occur at a designated microzone of the welded joints. The smooth flat specimen with a uniform gauge section shown in Fig. 2(a) and nominal strain approach were used to measure the LCF properties of Ti6Al4V for comparison. Because the local strain at the location of crack initiation has a significant effect on the low-cycle fatigue life, the nonuniform strain distribution near the notch root needs to be calculated through EPFEA. The EPFEA was modeled based on the gauge section of the notched flat specimen. The left end of the finite element model was fixed, and the right end was
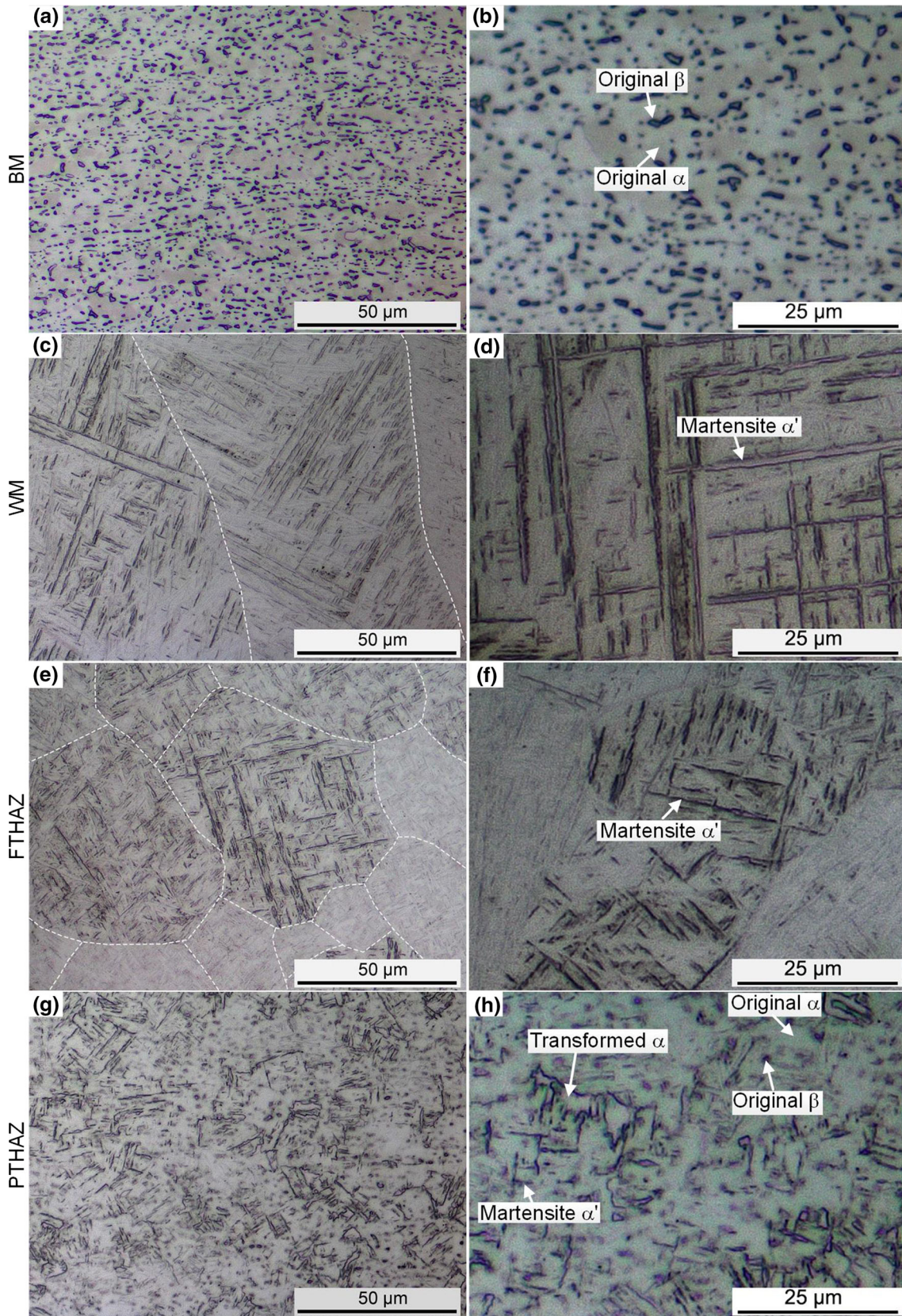
Fig. 4 Microstructures of the Ti6Al4V laser-welded joint. (a) and (b) BM, (c) and (d) WM, (e) and (f) FTHAZ, (g) and (h) PTHAZ

applied with the displacement. The displacement was specified with the corresponding nominal strain in the LCF tests. A global mesh size of 0.10 mm and refined mesh size of 0.05 mm

at the arc were selected. From the EPFEA results of the notched flat specimen for Ti6Al4V shown in Fig. 7, the stress and strain were concentrated in the notch root.

The strain at the notch root exceeds the nominal strain ε_n, as shown in the strain distributions along path AB in Fig. 7(c). Moreover, approximately 70% of the strain concentrates within the scope of 2 mm from the notch root for the notched flat Ti6Al4V specimen, as shown by the shadow in Fig. 7(c).

The fatigue results of the smooth and notched flat Ti6Al4V specimens are shown in Fig. 8. The fatigue property of the
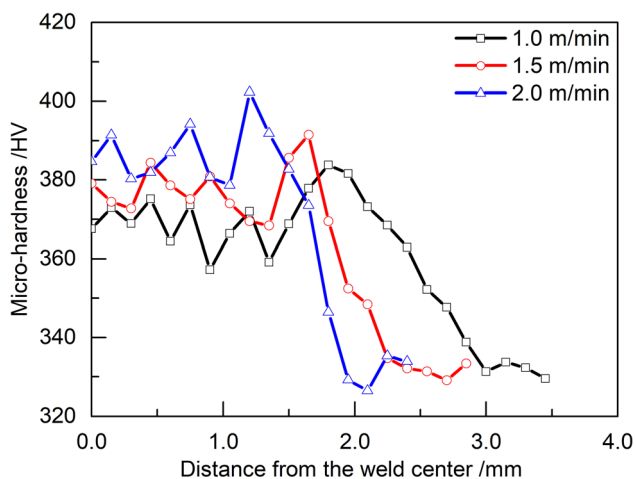
notched flat specimen using the nominal strain is conservative compared with the fatigue results of the smooth flat specimen, which indicates that the nominal strain is not suitable for the LCF assessment of the notched flat specimen. The fatigue results of the notched flat specimen using the local strain based on the local strain approach are close to the fatigue results of the smooth flat specimen. These results prove that the local strain approach is effective in the LCF assessment of the notched flat specimen regardless of the notch effect. The local strain is more suitable than the nominal strain for the LCF assessment of the notched flat specimen.

3.4 The LCF Properties of Ti6Al4V Laser-Welded Joints

The local strain approach was applied to estimate the LCF properties of the HAZ of Ti6Al4V laser-welded joints with three different welding speeds. Because of the heterogeneous material properties of welded joints, the Ti6Al4V laser-welded joint model was divided into different microzones, including the WM, FTHAZ, PTHAZ and BM. Each microzone was assigned corresponding elastic and plastic properties. As seen from the EPFEA results of the notched flat specimen of Ti6Al4V laser-welded joints shown in Fig. 9(a)–(c), the strain concentrates in the HAZ, which is located at the notch root of the notched flat specimen for welding speeds of 1.0 and 1.5 m·min^{-1}, and the strain concentrates in the HAZ/BM boundary for a welding speed of 2.0 m·min^{-1}. The strain distributions along the top edge (path AB) and bottom edge (path CD) shown in Fig. 9(b) of the welded joint with a welding speed of 1.5 m·min^{-1} under nominal strains of 0.006 and 0.010 are shown in Fig. 9(d). The difference between the strains along the top edge and bottom edge is small except for the strains near the notch root caused by the different sizes of the microzones on the top and bottom surfaces of the welded joints. The maximum strain of the bottom edge is larger than the maximum strain of the top edge. Therefore, the location of the maximum strain of the bottom edge is considered to be the location of fatigue crack initiation. The shapes of the strain curves at the bottom edge under nominal strains of 0.006 and 0.010 in Fig. 9(d) are similar. The strain curves of the bottom edge of welded joints with different welding speeds under a nominal strain of 0.010 are shown in Fig. 9(e)–(g). The

Fig. 5 Vickers microhardness of the laser-welded joints with different welding speeds
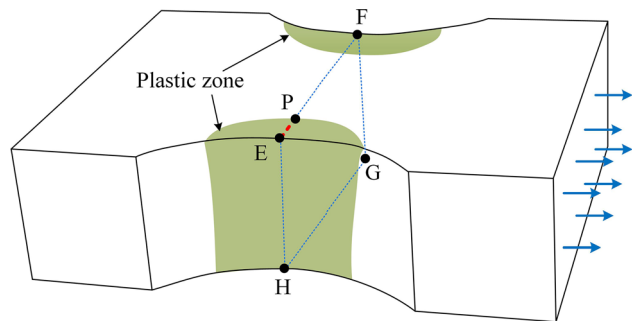

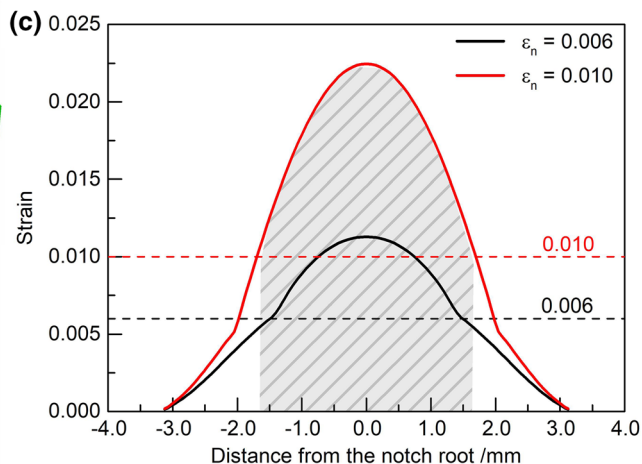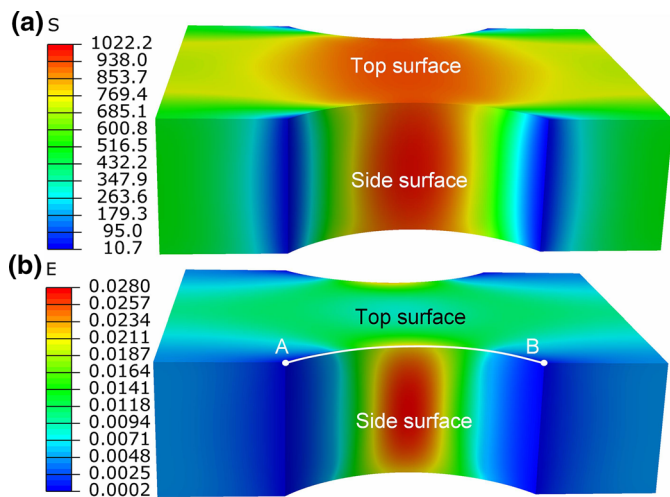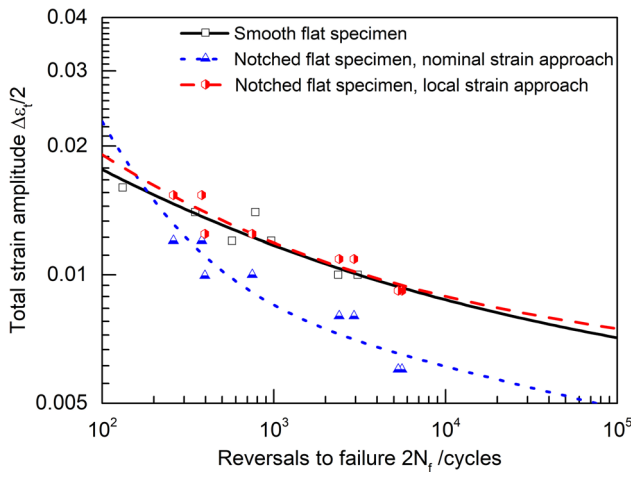**Fig. 6.** The definition of the local strain approach

Fig. 7 Local strains calculated by EPFEA of the notched flat specimen for Ti6Al4V: (a) and (b) stress and strain concentrations in the middle of the arc, and (c) strain distributions along path AB

Fig. 8 LCF assessment of the smooth and notched flat Ti6Al4V specimen based on the nominal strain and local strain approach
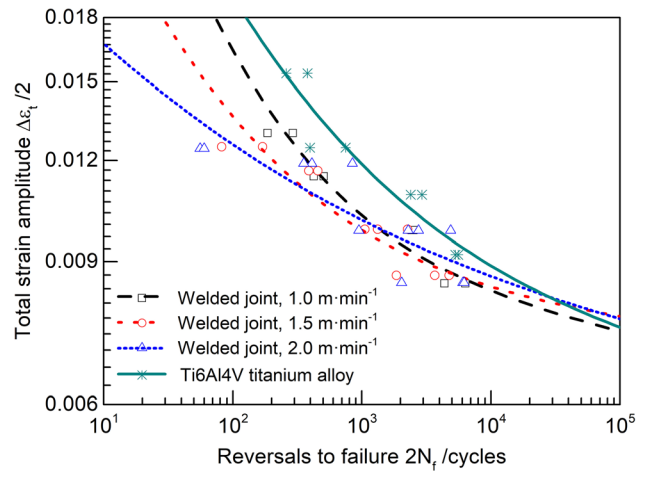
Fig. 10 Comparison of the LCF properties of Ti6Al4V and the HAZ of Ti6Al4V laser-welded joints with different welding speeds
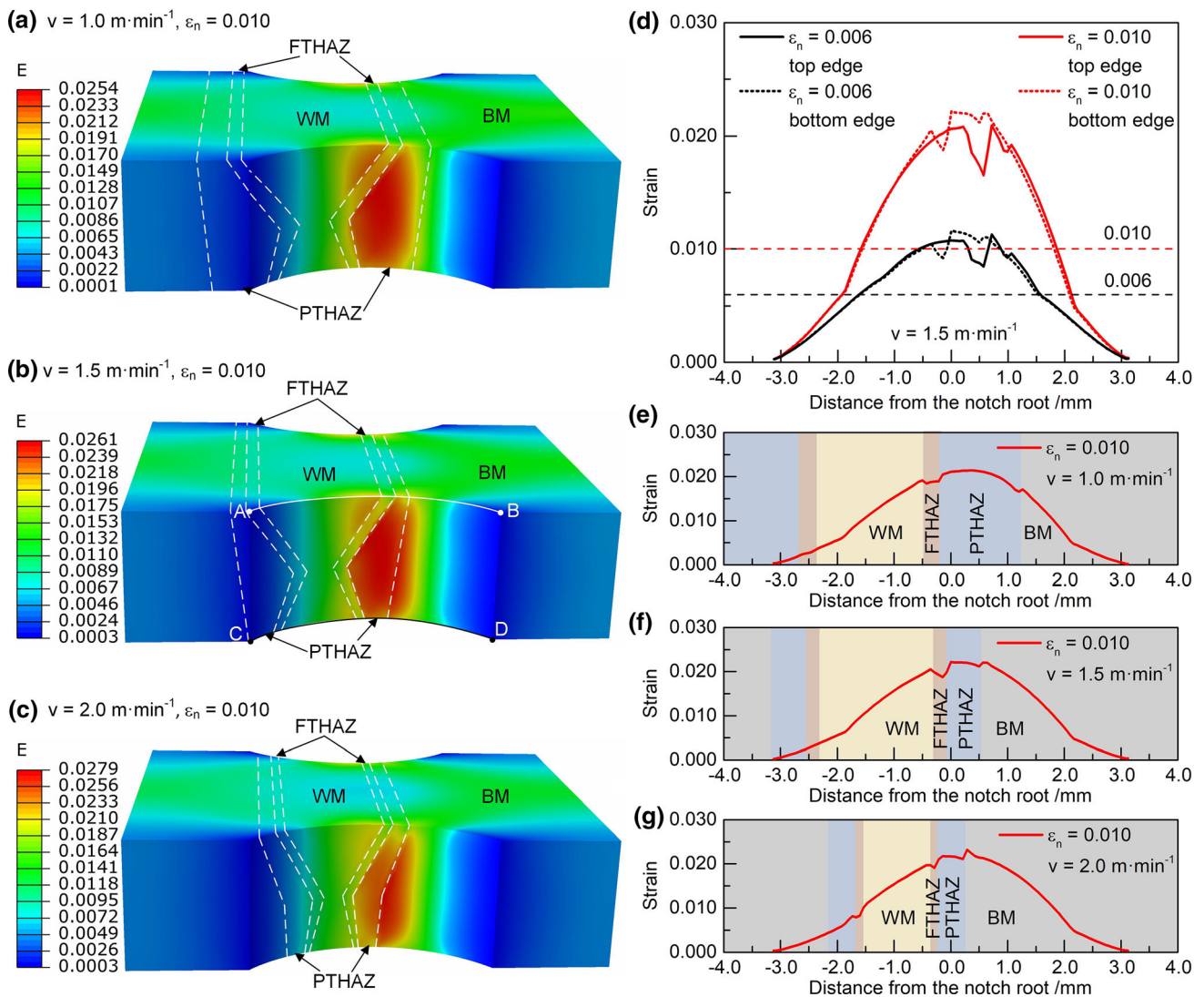

Fig. 9 Local strains of Ti6Al4V laser-welded joints with different welding speeds: (a), (b) and (c) strain concentrations, (d) strain distributions along the top edge (path AB) and bottom edge (path CD) of a welded joint, and (e), (f) and (g) strain distributions along the bottom edge of welded joints with different welding speeds.
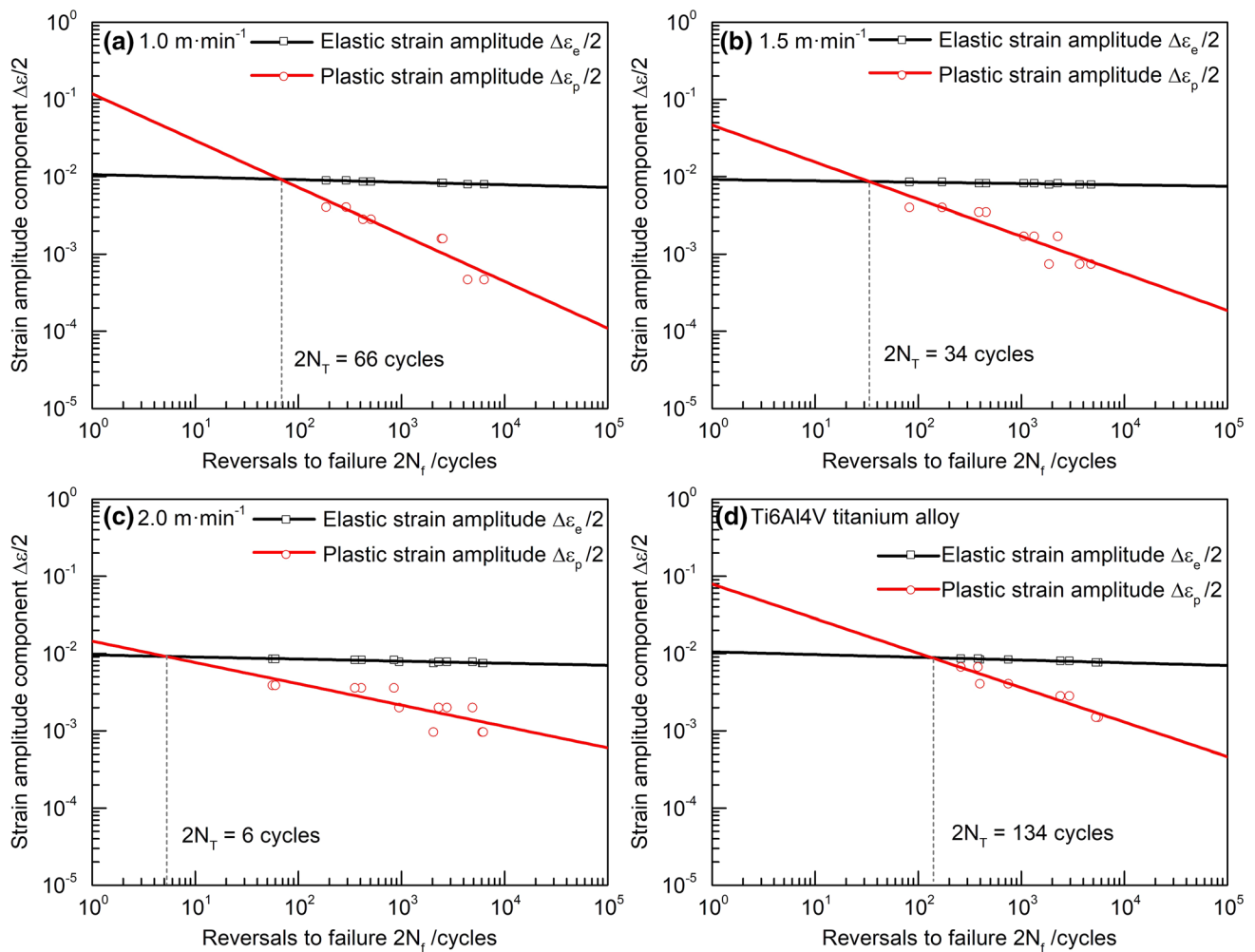
Fig. 11 Fatigue strength-life and fatigue ductility-life curves for (a), (b), and (c) Ti6Al4V laser-welded joints with welding speeds of 1.0, 1.5 and 2.0 m·min^{-1}, respectively, and (d) Ti6Al4V titanium alloy

maximum strain is located in the HAZ and within 0.5 mm of the notch root of the notched flat specimens for Ti6Al4V laser-welded joints.

The fatigue results of the notched flat specimens for Ti6Al4V titanium alloy (i.e., BM) and the HAZ of Ti6Al4V laser-welded joints based on the local strain approach are compared in Fig. 10. The LCF properties are better in the HAZ than in the BM for Ti6Al4V laser-welded joints. The LCF properties of the HAZ decrease with increasing welding speed.

The reasons why the LCF properties of the HAZ of Ti6Al4V laser-welded joints are worse than those of the BM are as follows. First, the microstructure and mechanical heterogeneity in the Ti6Al4V laser-welded joint cause stress and strain concentrations, leading to early microcracks in the Ti6Al4V laser-welded joint (Ref 22). Second, different microstructures between the BM and laser-welded joint cause different LCF properties. The LCF life of titanium alloy mainly depends on the resistance to short crack propagation (Ref 23). Birosca et al. (Ref 24) found that short cracks propagated along prismatic planes in the original α phase. The plastic deformation proceeded via the basal planes in the martensite α′ phase in Ti-V-Al alloy (Ref 25). The basal planes have only one orientation, and the prismatic planes have several orientations for the crack to propagate. The crack easily diverts in the

original α phase, leading to a better resistance to the short crack propagation for the original α phase than the martensite α′ phase. Therefore, the BM composed mostly of the original α phase has better LCF properties than the HAZ composed of large amounts of martensite α′ phase. Last, the ductility of the BM is higher than that of the WM and HAZ in Ti6Al4V laser-welded joints. The higher elastic-plastic transition life N_T of the Ti6Al4V compared with Ti6Al4V laser-welded joints in Fig. 11 also indicates that the ductility of Ti6Al4V is higher than the ductility of the HAZ in Ti6Al4V laser-welded joints.

When the strain amplitude is low, the influence of the elastic strain on LCF life is significant. The differences among the elastic properties of Ti6Al4V laser-welded joints with different welding speeds are small due to the similar chemical compositions. The similar elastic properties lead to the close LCF properties of the HAZ in Ti6Al4V laser-welded joints with different welding speeds under low strain levels, as shown in Fig. 10. When the strain amplitude is high, the influence of the ductility on the LCF properties is significant. As shown in Fig. 11, the elastic-plastic transition life N_T decreases with increasing welding speed, which indicates that the ductility of the HAZ in the Ti6Al4V laser-welded joint decreases with increasing welding speed. The weld hardening is higher for Ti6Al4V laser-welded joints with higher welding speed due to
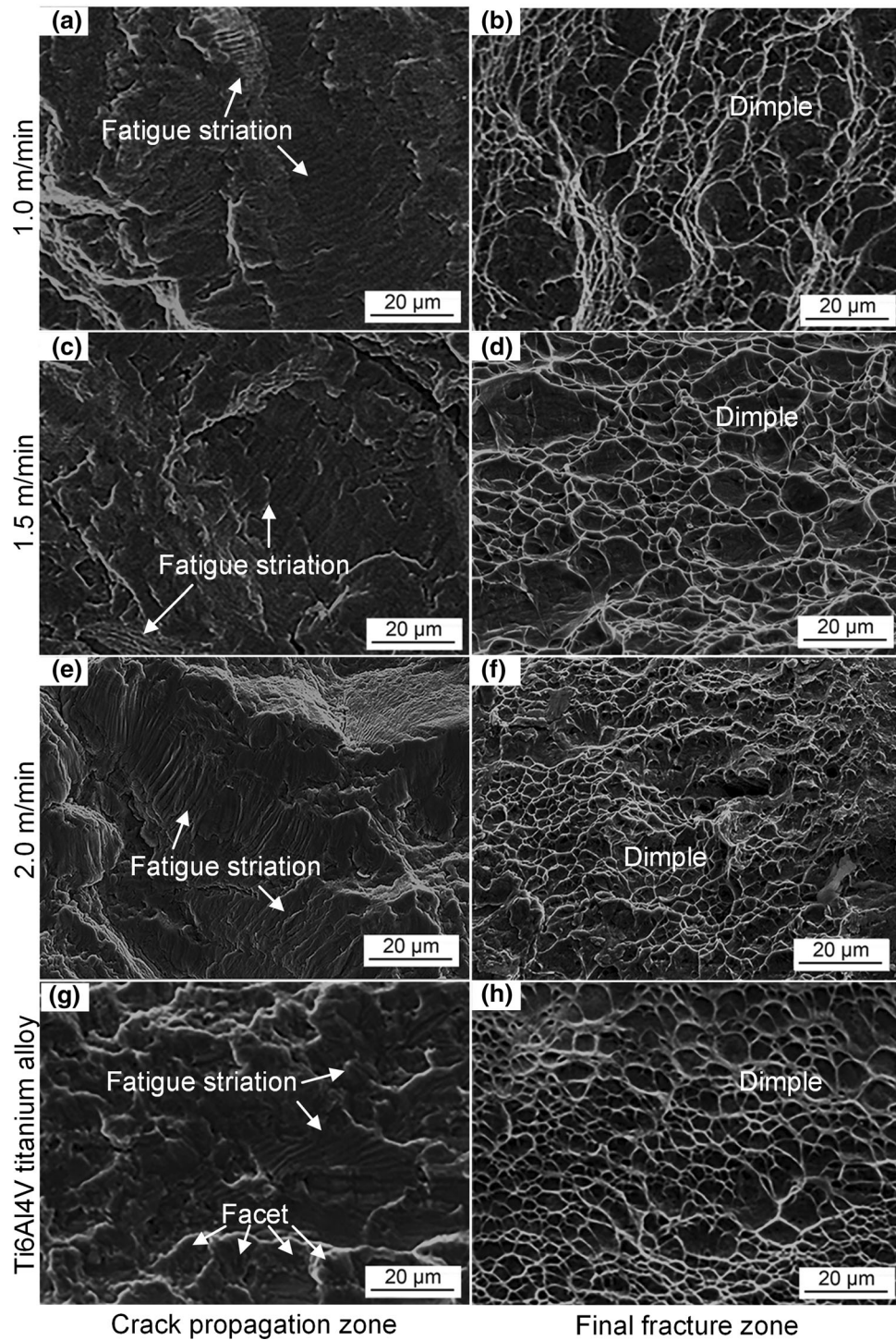
Fig. 12 SEM fractography of the Ti6Al4V titanium alloy and laser-welded joints with different welding speeds

the higher cooling rate (Ref 26), which results in a low ductility for welded joints with high welding speed. The worsened ductility is one of the main factors that cause diminished LCF properties for the Ti6Al4V laser-welded joints with high welding speed than low welding speed under high strain levels.

The LCF fractography of the Ti6Al4V titanium alloy and its laser-welded joints with different welding speeds are shown in Fig. 12. Fatigue striations can be observed in the crack propagation zone, and dimples can be observed in the final fracture zone for Ti6Al4V and its laser-welded joints. There are

many facets in the crack propagation zone, and the number of facets in the Ti6Al4V titanium alloy is greater than that in the Ti6Al4V laser-welded joints. The directions of the fatigue striations are different in different facets. The morphology and size of the facets of the Ti6Al4V titanium alloy are similar to the morphology and size of the original α phase. The small size and the different orientations of the original α phase in Ti6Al4V titanium alloy make the Ti6Al4V titanium alloy more resistant to crack propagation than the Ti6Al4V laser-welded joints. The widths of the fatigue striations of the Ti6Al4V titanium alloy

are larger than the widths of the fatigue striations. The widths of the fatigue striations decrease with increasing welding speed. This result also demonstrates that the ductility is better for the Ti6Al4V titanium alloy than for the Ti6Al4V laser-welded joints, and the ductility of the Ti6Al4V laser-welded joints decreases with the increase in welding speed.

4. Conclusions

(1) The local strain approach is proposed to estimate the LCF properties of a notched flat specimen. The local strain is defined as the average strain in the plastic zone and critical section of the notched flat specimen. The local strain changes with the fatigue load and can be calculated through EPFEA.

(2) Because of the low ductility caused by the martensite microstructure in the HAZ and mechanical heterogeneity in the welded joints, the LCF properties of Ti6Al4V laser-welded joints are worse in the HAZ than in the BM.

(3) The LCF properties are close for Ti6Al4V laser-welded joints with different welding speeds under low strain levels due to the close elastic properties. Due to the decrease in ductility caused by the high cooling rate for a high welding speed, the LCF properties of a Ti6Al4V laser-welded joint decrease with increasing welding speed under high strain levels.

References:

1. G. Casalino, M. Mortello and S.L. Campanelli, Ytterbium Fiber Laser Welding of Ti6Al4V Alloy, *J. Manuf. Process.*, 2015, **20**, p 250–256

2. F. Caiazzo, F. Curcio, G. Daurelio et al., Ti6Al4V Sheets Lap and Butt Joints Carried Out by CO_2 Laser: Mechanical and Morphological Characterization, *J. Mater. Process. Technol.*, 2004, **149**, p 546–552

3. X. Gao, J. Liu, L. Zhang et al., Effect of the Overlapping Factor on the Microstructure and Mechanical Properties of Pulsed Nd:YAG Laser Welded Ti6Al4V Sheets, *Mater. Charact.*, 2014, **93**, p 136–149

4. A. Squillace, U. Prisco, S. Ciliberto et al., Effect of Welding Parameters on Morphology and Mechanical Properties of Ti-6Al-4V Laser Beam Welded Butt Joints, *J. Mater. Process. Technol.*, 2012, **212**, p 427–436

5. C. Köse and E. Karaca, Robotic Nd:YAG Fiber Laser Welding of Ti-6Al-4V Alloy, *Metals*, 2017, **7**(6), p 221

6. J. Liu, X. Gao and J. Zhang, Effect of Heat Input on the Tensile Damage Evolution in Pulsed Laser Welded Ti6Al4V Titanium Sheets, *J. Mater. Eng. Perform.*, 2016, **25**(11), p 5109–5124

7. J.C. Stinville, F. Bridier, D. Ponsen et al., High and Low Cycle Fatigue Behavior of Linear Friction Welded Ti-6Al-4V, *Int. J. Fatigue*, 2015, **70**, p 278–288

8. B. Möller, J. Baumgartner, R. Wagener et al., Low Cycle Fatigue Life Assessment of Welded High-Strength Structural Steels Based on Nominal and Local Design Concepts, *Int. J. Fatigue*, 2017, **101**, p 192–208

9. T. Bruder, K. Störzel, J. Baumgartner et al., Evaluation of Nominal and Local Stress Based Approaches for the Fatigue Assessment of Seam Welds, *Int. J. Fatigue*, 2012, **34**(1), p 86–102

10. D.B. Lanning, T. Nicholas and G.K. Haritos, On the Use of Critical Distance Theories for the Prediction of the High Cycle Fatigue Limit Stress in Notched Ti-6Al-4V, *Int. J. Fatigue*, 2005, **27**, p 45–57

11. X. Hu, X. Jia, Z. Bao et al., Effect of Notch Geometry on the Fatigue Strength and Critical Distance of TC4 Titanium Alloy, *J. Mech. Sci. Technol.*, 2017, **31**(10), p 4727–4737

12. K. Saiprasertkit, T. Hanji and C. Miki, Fatigue Strength Assessment of Load-Carrying Cruciform Joints with Material Mismatching in Low- and High-Cycle Fatigue Regions Based on the Effective Notch Concept, *Int. J. Fatigue*, 2012, **40**, p 120–128

13. R. Sandhya, A. Veeramani, K.B.S. Rao et al., On Specimen Geometry Effects in Strain-Controlled Low-Cycle Fatigue, *Int. J. Fatigue*, 1994, **16**(3), p 202–208

14. Y. Besel, M. Besel, E. Dietrich et al., Heterogeneous Local Straining Behavior Under Monotonic and Cyclic Loadings in a Friction Stir Welded Aluminum Alloy, *Int. J. Fatigue*, 2019, **125**, p 138–148

15. K. Tateishi and T. Hanji, Low Cycle Fatigue Strength of Butt-Welded Steel Joint by Means of New Testing System with Image Technique, *Int. J. Fatigue*, 2004, **26**(12), p 1349–1356

16. B. Karabulut, G. Lombaert, D. Debruyne et al., Experimental and Numerical Fatigue Assessment of Duplex Welded Transversal Stiffeners, *Int. J. Fatigue*, 2020, **134**, p 105498

17. J.R. Cahoon, An Improved Equation Relating Hardness to Ultimate Strength, *Metall. Trans.*, 1972, **3**(11), p 3040

18. J.S. Keist and T.A. Palmer, Development of Strength-Hardness Relationships in Additively Manufactured Titanium Alloys, *Mater. Sci. Eng. A*, 2017, **693**, p 214–224

19. W. Lu, Y. Shi, X. Li et al., Correlation Between Tensile Strength and Hardness of Electron Beam Welded TC4-DT Joints, *J. Mater. Eng. Perform.*, 2013, **22**(6), p 1694–1700

20. Z. Xu, Z. Dong, Z. Yu et al., Relationships between microhardness, Microstructure, and Grain Orientation in Laser-Welded Joints with Different Welding Speeds for Ti6Al4V Titanium Alloy, *Trans. Nonferrous Met. Soc. China*, 2020, **30**(5), p 1277–1289

21. J.R. Cahoon, W.H. Broughton, and A.R. Kutzak, The Determination of Yield Strength from Hardness Measurements, *Metall. Trans.*, 1971, **2**(7), p 1979–1983

22. J. Liu, X. Gao, L. Zhang et al., A Study of Fatigue Damage Evolution on Pulsed Nd:YAG Ti6Al4V Laser Welded joints, *Eng. Fract. Mech.*, 2014, **117**, p 84–93

23. C. Leyens and M. Peters, *Titanium and Titanium Alloys: Fundamentals and Applications*, John Wiley & Sons, 2003

24. S. Birosca, J.Y. Buffiere, M. Karadge et al., 3-D Observations of Short Fatigue Crack Interaction with Lamellar and Duplex Microstructures in a Two-Phase Titanium Alloy, *Acta Mater.*, 2011, **59**(4), p 1510–1522

25. H. Matsumoto, H. Yoneda, D. Fabregue et al., Mechanical Behaviors of Ti-V-(Al, Sn) Alloys with α′ Martensite Microstructure, *J. Alloys Compd.*, 2011, **509**(6), p 2684–2692

26. K. Hong and Y.C. Shin, Analysis of Microstructure and Mechanical Properties Change in Laser Welding of Ti6Al4V with a Multiphysics Prediction Model, *J. Mater. Process. Technol.*, 2016, **237**, p 420–429

Publisher's Note Springer Nature remains neutral with regard to jurisdictional claims in published maps and institutional affiliations.